CHEMISTRY OF MATERIALS

ARTICLE

pubs.acs.org/cm

Systematic Pore-Size Effects of Nanoconfinement of $LiBH_4$: Elimination of Diborane Release and Tunable Behavior for Hydrogen Storage Applications

Xiangfeng Liu,[†] David Peaslee,[†] Christopher Z. Jost,[†] Theodore F. Baumann,[‡] and Eric H. Majzoub*[,†]

[†]Center for Nanoscience and Department of Physics and Astronomy, University of Missouri-St. Louis, One University Boulevard, St. Louis, Missouri 63121, United States

[‡]Lawrence Livermore National Laboratory, Livermore, California, United States

Supporting Information

ABSTRACT: The effects of nanoconfinement on the structural phase transition, H_2 release and uptake, and the emission of toxic diborane (B_2H_6) on desorption of $LiBH_4$ have been comprehensively investigated in the presence of various porous hard carbon templates at a variety of pore sizes. Calorimetry signatures of both the structural phase transition and melting of nanoconfined $LiBH_4$ shifted to a lower temperature with respect to the bulk, finally vanishing below a pore size around 4 nm. The desorption of $LiBH_4$ confined in these nanoporous carbons shows a systematic and monotonic decrease in the desorption temperature and concomitantly, mass spectroscopic analysis indicated a gradual reduction of the partial pressure of B_2H_6 with decreasing pore size, suggesting that formation of stable closoborane salts may be avoided by interrupting the reaction pathway. This represents a major breakthrough in the reversibility of boron-based hydrogen storage systems, where capacity is lost in the formation of stable B−H species on cycling. Different carbon preparation techniques suggest that the confinement size, and not solely surface interactions, may be used to tune the properties of complex hydrides for kinetic and reaction pathway improvements for hydrogen storage applications.

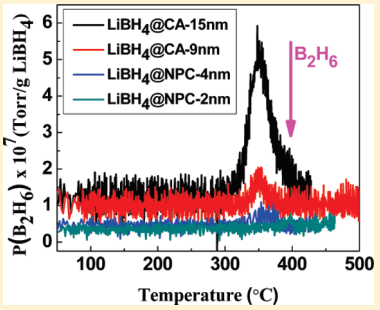

KEYWORDS: hydrogen storage, borohydride, nanoconfinement, porous carbon

INTRODUCTION

Hydrogen storage is one of the key technical barriers to the widespread commercialization of hydrogen-fueled vehicles.[1,2] Among the current hydrogen storage technologies,[3−5] complex metal hydrides have received wide attention due to their high gravimetric H_2 capacity.[6] Bulk lithium borohydride ($LiBH_4$) has a gravimetric capacity of 18.5 wt %, but its poor hydrogen release/uptake kinetics and impractical reversibility conditions restrict its application as hydrogen storage medium. $LiBH_4$ decomposes at around 500 °C and the dehydrided products can be rehydrided at 350 bar H_2 and 600 °C.[7] In addition, the evolution of diborane (B_2H_6) accompanying H_2 release during the decomposition of $LiBH_4$ results in capacity loss on each cycle, and is also a safety concern.[8−11] A few approaches have been applied to improve the dehydrogenation kinetics and the reversibility of $LiBH_4$ such as the addition of catalysts or destabilizers.[12−16] Vajo et al. found the addition of MgH_2 to $LiBH_4$ lowered the hydrogenation/dehydrogenation enthalpy by 25 kJ/(mol of H_2) compared with pure $LiBH_4$ and improved the reversibility.[12] However, this destabilization strategy relies on the formation of the very stable compound MgB_2 on decomposition, limiting reversibility to high temperatures. Yang et al. studied the destabilization of $LiBH_4$ by adding metals (Mg, Al, Ti, V, Cr, or Sc) or metal hydrides like MgH_2, TiH_2, or CaH_2.[13] Au et al. improved the reversibility of $LiBH_4$ by ball milling with some transition metal oxides or chlorides and moderated the rehydrogenation conditions to 873 K and 7 MPa.[14] But the rehydrogenation temperature is still too high for practical applications. The formation of diborane during the decomposition of the composite systems remains a persistent problem, and cannot be understated. One of the largest obstacles to the use of boron-based hydrogen storage systems is the formation of stable "sinks" of, for example, closoborane $[B_{10}H_{10}]^{2-}$ and $[B_{12}H_{12}]^{2-}$ salts,[9,10] that decrease capacity as boron is lost to these compounds on each cycle. Hwang et al. confirmed the presence of intermediate $Li_2B_{12}H_{12}$ on the decomposition of $LiBH_4$ by ^{11}B NMR.[9] A more recent study showed that $Li_2B_{12}H_{12}$ and possibly $Li_2B_{10}H_{10}$ resulted from the reaction of the released B_2H_6 with the remaining $LiBH_4$ on decomposition.[17] We show below that the intermediates needed for the formation of the closoboranes are not produced if the confinement size is small enough, representing a breakthrough in the utilization of boron-based hydrogen storage systems.

Recently, nanoconfinement of hydrides has proven beneficial in hydrogen storage materials and may provide new insights and

Received: December 13, 2010
Revised: January 19, 2011
Published: February 08, 2011

solutions to current hydrogen storage technology.[18−22] Theoretical calculations and preliminary experiments show that nanosized metal hydrides have significantly different thermodynamic and kinetic properties with respect to their bulk counterparts. First-principles density functional theory (DFT) calculations indicate the H_2 desorption enthalpy for MgH_2 may be substantially decreased when the particle size becomes very small (~1.3 nm).[23] Paskevicius et al. investigated the thermodynamic properties of magnesium hydride nanoparticles (~7 nm in size) and found only a small decrease in the decomposition reaction enthalpy of about 3 kJ/mol H_2.[24] However, the complex hydride $NaAlH_4$ embedded in microporous carbon fiber shows a dramatic change in the resulting pressure−composition−isotherm suggesting large changes in thermodynamic properties and perhaps the reaction pathway.[25] Gao et al. also reported that the confinement of $NaAlH_4$ in porous carbons with 2−3 nm pores improved both the kinetics and thermodynamics of hydrogen sorption.[26]

The improved kinetics and perhaps thermodynamics of nanoconfined hydrides have attracted increasing interest in improving the properties of $LiBH_4$.[27−30] Vajo and co-workers enhanced the dehydrogenation kinetics and reversibility through infiltrating $LiBH_4$ into carbon aerogels (CA). The reported desorption rate at 300 °C of $LiBH_4$ confined in the CA host was 50 times faster than bulk and the dehydrided sample was rehydrided at 100 bar H_2 and 400 °C.[27] More recently, Jensen's group reported the hydrogen storage properties of nanoconfined MgH_2 and $LiBH_4/MgH_2$ in carbon aerogels ($D_{max} \approx$ 21 nm).[31] These nanoconfined systems showed significantly enhanced desorption kinetics and possibly improved thermodynamic properties. In a recent publication, our group reported the decomposition properties of nanoconfined $LiBH_4$ in highly ordered hexagonally packed cylindrical nanoporous carbon (NPC) with an average pore size of 2.0 nm and a very narrow size distribution.[32] The nanoconfined $LiBH_4$ in such small pores resulted in the disappearance of the low temperature structural phase transition, the melting transition, and also the significant decrease of the onset desorption temperature from 460 to 220 °C with respect to bulk $LiBH_4$. Most importantly, diborane release of $LiBH_4$ confined in the highly ordered nanoporous carbon was suppressed or eliminated in the decomposition indicating a changed decomposition pathway. However, the studies above lack a direct set of systematic measurements of these properties on pore, and ultimately, particle size of the hydride. In this report, we present a comprehensive study of the effects of nanoconfinement size on the calorimetry, diborane emission and reversibility of $LiBH_4$ through a series of experiments on both CAs and highly ordered nanoporous carbons with a pore size distribution from 2 to 15 nm.

EXPERIMENTAL SECTION

Highly ordered porous carbons were prepared according to a well-established method.[33] The preparation conditions of NPC-2 nm also can be found in an earlier publication.[32] The preparation method of NPC-4 nm was similar to NPC-2 nm except that NPC-4 nm was calcinated at 600 °C under a flowing O_2/N_2 (O_2: 2.5 vol %). NPC-L represents the NPC with lower surface area. The preparation of NPC-L is similar to NPC-2 nm except that it was not crushed to powders before calcination. The CAs used in this study were prepared through carbonization of organic aerogels derived from resorcinol and formaldehyde. Resorcinol (99%), formaldehyde (37% in water) and sodium carbonate monohydrate reagents were purchased from Aldrich Chemical Co. and used without further purification. For the synthesis of the CA with 9 nm pores, resorcinol (12.35 g, 112 mmol) and 37% formaldehyde solution (17.9 g, 224 mmol) were dissolved in distilled water (32 mL), followed by the addition of sodium carbonate monohydrate (0.069 g, 0.55 mmol). The same reactant ratio was employed for the synthesis of the CA scaffold with 15 nm pores with the exception that a larger volume of distilled water (62 mL) was used in the reaction. These reaction mixtures were then transferred to cylindrical glass molds and cured at 80 °C for 72 h. The resultant organic hydrogels were washed with acetone to remove the water from the pores of the gel and then dried with supercritical CO_2 (T_c = 31.1 °C, P_c = 7.4 MPa). The organic aerogels were subsequently carbonized at 1050 °C (ramp rate: 2 °C/min) for 3 h under an N_2 atmosphere, affording the CAs as black cylindrical monoliths. The porous carbon templates were first dried at 900 °C for 5 h under flowing Ar and then dried at 400 °C under vacuum. Subsequently, the dried carbons were impregnated with $LiBH_4$ by a melting method. In a typical process, a 200 mg mixture of $LiBH_4$ (95%, Aldrich) and carbon template was loaded into a sample holder in an argon-filled glovebox. The sample holder was subsequently attached to a fixed-volume Sievert's-type instrument without exposing the sample to air. The sample holder was heated to 300 °C under about 60 bar H_2 then kept at this temperature for 30 min. These premelted samples are hereafter referred to as $LiBH_4$@CA-x or $LiBH_4$@NPC-x (x: the values at the pore size distribution peaks.).

Textural properties of carbon aerogels were determined using N_2 adsorption−desorption techniques (ASAP 2010 Surface Area Analyzer, Micromeritics). Brunauer−Emmett−Teller (BET) and Barrett−Joyner−Halenda (BJH) methods were used to calculate surface areas and pore size distributions using desorption data, respectively. An SA3100 analyzer (Coulter) was used to measure nitrogen adsorption isotherms for NPC carbons at 77 K. Before analysis, the sample of porous carbon was outgassed for 1 h at 300 °C under a vacuum. The BET method was used to calculate the specific surface areas (S_{BET}) using adsorption data in a relative pressure range from 0.05 to 0.2 bar. The total pore volume was estimated from the adsorbed amount at a relative pressure P/P_0 of 0.98 based on the BJH model. The morphology of the nanoporous carbon was investigated using a Philips EM430 high-resolution transmission electron microscopy (TEM). The powder was supported on the copper grid coated by a carbon film. X-ray diffraction (XRD) was performed on a Rigaku Ultima IV multipurpose X-ray diffraction (XRD) system with CuK_a radiation source. Samples containing hydrides were covered with parafilms to prevent the samples from contacting air or moisture during the XRD experiments. FT-IR spectra were collected using Nicolet 6700. Two KBr polished discs were used to hold the powered samples. Differential scanning calorimetry (DSC) analysis was performed on a TQ2000 series analyzer (TA Instruments). About 4 mg of sample was loaded in a Tzero pan in an argon-filled glovebox and crimped with a Tzero lid. The sample was heated to 550 °C at a ramping rate of 10 °C/min under a N_2 flowing rate of 50 mL/min. Thermogravimetric analysis (TGA) was performed on a TGAQ500 Series thermogravimetric analyzer (TA Instruments). In a typical TGA procedure, about 10 mg of sample was loaded in a Tzero pan and crimped with a Tzero hermetic lid in an argon-filled glovebox. A hermetic lid was selected to reduce contamination and a pinhole was made on the top of the lid for the purpose of H_2 release. The sample was heated to 550 °C at a ramping rate of 10 °C/min under a N_2 flowing rate of 100 mL/min. Mass spectroscopic analysis was performed using an SRS RGA200 residual gas analyzer (RGA) and a high temperature sample stage. The system is separated into a HV (1×10^{-8} to 1×10^{-5} Torr) sample chamber and UHV (1×10^{-9} to 1×10^{-7} Torr) gas analysis chamber. The species partial pressure per gram of $LiBH_4$ was used for comparisons. The details of the measurement can be found in an earlier publication.[32]

RESULTS AND DISCUSSION

TEM was used to characterize the pore structure. Figure 1 shows TEM images of columnar pores packed in a hexagonal

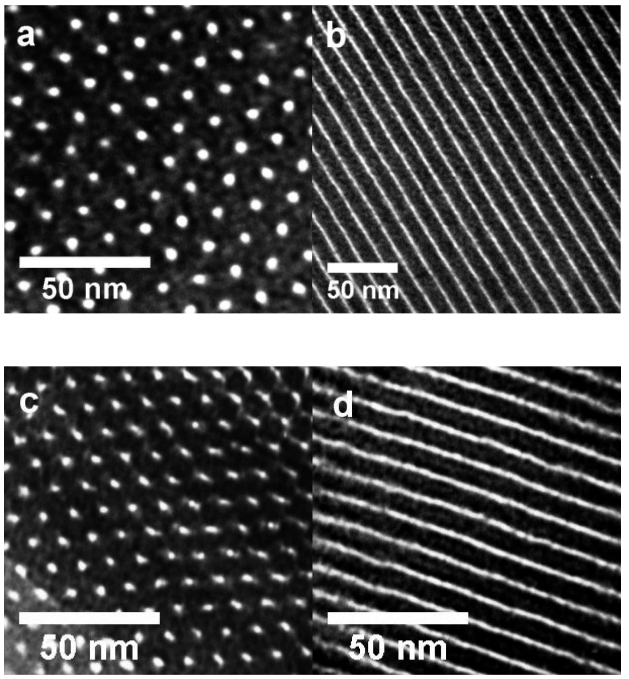

Figure 1. TEM images of columnar pores packed in a hexagonal geometry for (a, b) NPC-4 nm and (c, d) NPC-L viewed from the directions parallel (a, c) and perpendicular (b, d) to the pore channels.

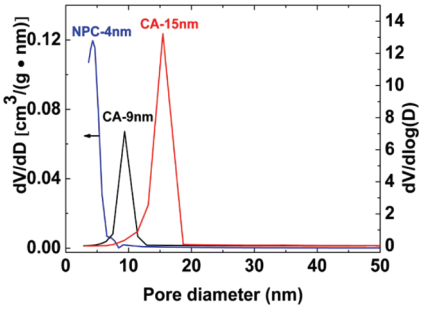

Figure 2. Pore-size distributions of NPC-4 nm, CA-9 nm, and CA-15 nm. Pore-size distributions of carbon aerogels were analyzed by ASAP 2010 surface area analyzer (Micromeritics) based on the desorption data. Pore-size distribution of NPC was analyzed by SA3100 analyzer (Coulter) based on adsorption isotherms.

geometry for NPC-4 nm (a, b) and NPC-L (c, d) viewed from the directions parallel (a, c) and perpendicular (b, d) to the pore channels. From TEM images, we can clearly see the highly ordered hexagonally packed pores viewed from the direction parallel to the pore channels [001] and stripe-like patterns viewed from the direction perpendicular to the pore channels [110], respectively, in good agreement with the previously reported pore morphology.[32,33]

Figure 2 shows the pore size distributions of CA-15 nm, CA-9 nm and NPC-4 nm. The pore size of 15, 9, and 4 nm correspond to the values at the pore size distribution peaks. The two carbon aerogels both have a slightly wider pore size distribution in comparison with the ordered porous carbon. The surface area and the total pore volumes are summarized in Table 1.

Table 1. Surface Areas and the Total Pore Volumes of Different Carbon Templates

samples	CA-15 nm	CA-9 nm	NPC-4 nm	NPC-2 nm	NPC-L
BET surface area (m^2/g)	652	706	730	594	241
total pore volume (cm^3/g)	2.3	1.5	0.53	0.35	0.13

The specific surface areas (S_{BET}) of NPC-4 nm based on the BET method and the total pore volume calculated by the BJH model were 730 m^2/g and 0.53 cm^3/g, respectively. S_{BET} and the total pore volume of $LiBH_4$@NPC-4 nm were reduced to 292 m^2/g and 0.23 cm^3/g, respectively, indicating the filling or blocking of the pores by $LiBH_4$ (see Figure S1 in the Supporting Information).

In an earlier publication we have shown that $LiBH_4$ confined in NPC-2 nm is amorphous and shows no Bragg peaks of $LiBH_4$.[32] Similarly, the XRD pattern of the premelted $LiBH_4$@NPC-4 nm also does not show Bragg peaks of $LiBH_4$, indicating the hydride became amorphous after melt-infiltration in the 4 nm nanopores (see Figure S2 in the Supporting Information). In contrast, the XRD pattern of $LiBH_4$@CA-9 nm shows peaks indicating the existence of crystalline $LiBH_4$. However, the confinement of the hydride in 9 nm pores still results in broad and diffuse Bragg peaks. Fourier transform infrared spectroscopy was further used to confirm the existence of $[BH_4^-]$ in the infiltrated sample of $LiBH_4$@NPC-4 nm. The spectra indicate B−H bending modes at 1100 cm^{-1} and stretching modes around 2200−2300 cm^{-1} of $[BH_4^-]$ (see Figure S3 in the Supporting Information).

DSC plots of bulk $LiBH_4$ and nanoconfined $LiBH_4$@NPC or $LiBH_4$@CA are shown in Figure 3. The DSC plot of bulk $LiBH_4$ shows the orthorhombic to hexagonal structure transition at a temperature of about 115 °C, melting at 284 °C and a decomposition peak around 495 °C. Both the structural phase transition and the melting transition of the nanoconfined $LiBH_4$ in carbon aerogels (CA-9 nm and CA-15 nm) still appeared but the transition peaks became broader and shifted to a lower temperature with decreasing pore size. The DSC trace of the structural phase transition is broader in bulk $LiBH_4$ than in infiltrated samples. (If we assume the phase transition proceeds by a nucleation and growth process, and if the nucleation is heterogeneous and more likely to occur on the large surface area of the templates, it would take a shorter time to complete the phase transition in the infiltrated samples, in agreement with the experimental results.) The appearance of the structural phase transition and the melting transition indicates the existence of crystalline $LiBH_4$ in agreement with XRD analysis. The broadness and temperature shift of the transition peaks is attributed to the decreasing coherence length within the incorporated material from nanoconfinement effects. In contrast, neither the structural transition or melting peak appeared in $LiBH_4$@NPC (2 or 4 nm) indicating $LiBH_4$ confined in the ordered NPC becomes amorphous as indicated in XRD analysis. We note that two small broad endothermic peaks appeared at about 80 and 200 °C when the loading of $LiBH_4$ in NPC-4 nm was increased to 20 wt %, where about 70% of the pore volume was filled, and may be due to incomplete infiltration of the LiBH4 into the pores (see Figure 5 below).

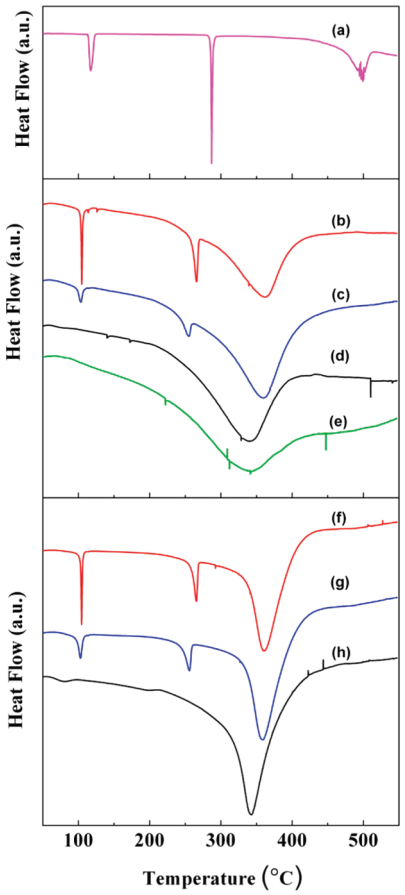

Figure 3. DSC plots of bulk $LiBH_4$ and nanoconfined $LiBH_4$@NPC or $LiBH_4$@CA: (a) bulk $LiBH_4$; (b) $LiBH_4$@CA-15 nm with a loading of 10 wt %; (c) $LiBH_4$@CA-9 nm with a loading of 10 wt %; (d) $LiBH_4$@NPC-4 nm with a loading of 10 wt %; (e) $LiBH_4$@NPC-2 nm with a loading of 10 wt %; (f) $LiBH_4$@CA-15 nm with a loading of 20 wt %; (g) $LiBH_4$@CA-9 nm with a loading of 20 wt %; (h) $LiBH_4$@NPC-4 nm with a loading of 20 wt %.

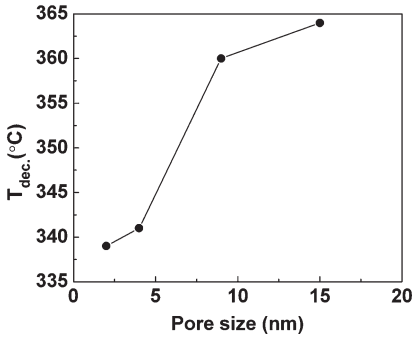

Figure 4. Pore-size dependence of dehydrogenation temperature of nanoconfined $LiBH_4$ in different carbon templates with a loading of 10 wt %. The lines connecting the points are only a guide for the eye.

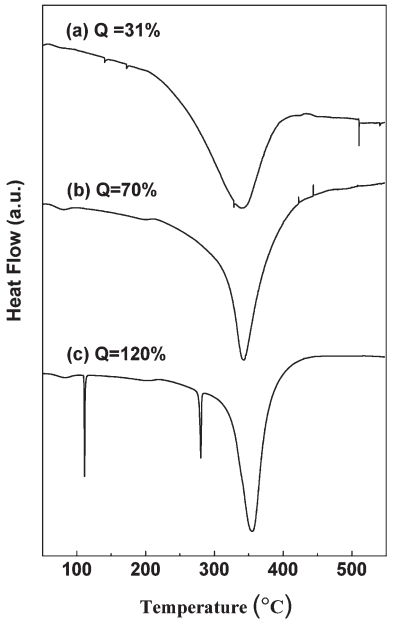

Figure 5. Comparisons of DSC plots for $LiBH_4$@NPC-4 nm with different filling degree. Q represents the filling degree of the pore by $LiBH_4$. $Q = V_{hydride}/V_{total}$ ($V_{hydride}$ and V_{total} represent the volume of hydrides and total pore volume, respectively).

Figure 4 shows the temperature of maximum hydrogen release rate, as determined from both TGA and DSC measurements, versus pore size. In comparison with the bulk $LiBH_4$ the dehydrogenation temperature of $LiBH_4$ confined in the carbon templates tends to decrease more with the decrease of the pore size. Note that the dehydrogenation temperature does not decrease linearly with the decreasing pore size; there is a sharp decrease in desorption temperature when the pore size is reduced from 9 to 4 nm, which may be attributed to the fact that $LiBH_4$ confined in 4 nm templates becomes amorphous.

Thermogravimetric analysis (TGA) was further used to study the dehydrogenation behaviors of the samples and is shown in the Supporting Information. Figure S4a shows the thermogravimetric and the corresponding DSC plots of $LiBH_4$@NPC-4 nm, which starts to decompose below the melting point. The fastest dehydrogenation appeared around 342 °C in agreement with the endothermic peak in DSC. Figure S4b compares the thermogravimetric plots of $LiBH_4$@NPC-4 nm and $LiBH_4$@CA-9 nm, indicating $LiBH_4$@NPC-4 nm has a lower dehydrogenation temperature.

The extent to which the pore volume can be filled while retaining the benefits of confinement was studied by varying the filling factor of $LiBH_4$ in the pores. We denote by Q the filling factor of the pores with $LiBH_4$, with $Q = 100\%$ corresponding to a maximum loading of 26 wt % (for $LiBH_4$@NPC-4 nm), based on the pore volume and density of crystalline orthorhombic $LiBH_4$. Figure 5 shows the DSC plots of $LiBH_4$@NPC-4 nm with different Q. When the content of $LiBH_4$ in NPC was 10 wt % ($Q = 31\%$) no structural transition or melting transition appeared. When the loading was increased to 30 wt % ($Q = 120\%$), and the template was significantly overfilled, both the structural, and melting transition appeared, indicating lack of available pore space. At $Q = 70\%$, small endothermic signatures are present, indicating that some $LiBH_4$ may be exterior to the pores, and may represent the practical limit of pore loading in this NPC.

Nanoconfinement is thought to improve the reversibility of hydrides due to limitation of the diffusion of the decomposing species.[19] Although bulk $LiBH_4$ can be rehydrided at 350 bar H_2 and 600 °C,[7] nanoconfined $LiBH_4$ in carbon aerogels with a pore size of 13 and 25 nm can be rehydrided at significantly lower temperatures and pressures of 100 bar H_2 and 400 °C.[27]

dx.doi.org/10.1021/cm103546g |*Chem. Mater.* 2011, 23, 1331–1336

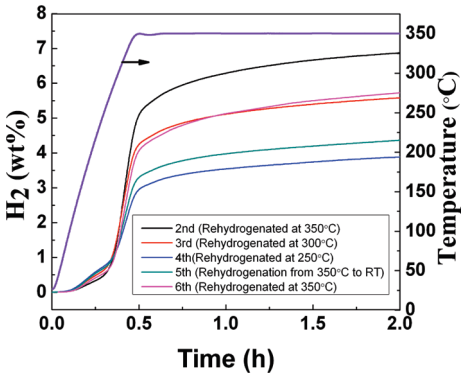

Figure 6. Desorption curves of nanoconfined $LiBH_4$@NPC-4 nm with an initial loading of 20 wt % ($Q = 70\%$).

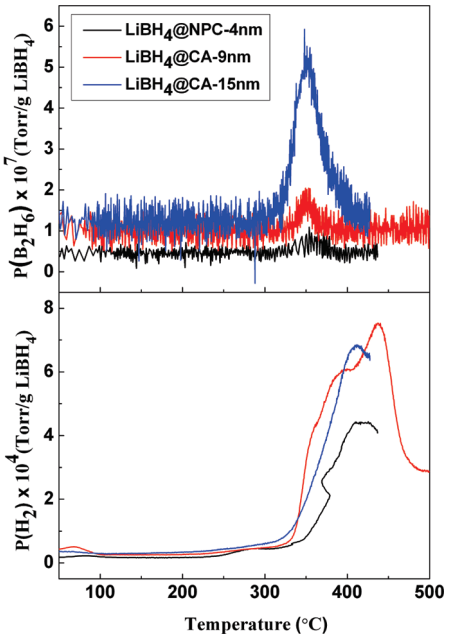

Figure 7. B_2H_6 and H_2 release with increasing temperature for $LiBH_4$@NPC-4 nm, LiBH4@CA-9 nm, and $LiBH_4$@CA-15 nm. The loading of each sample is 10 wt %.

As discussed in the section below, $LiBH_4$@NPC-4 nm desorbs and also absorbs under moderate conditions below the melting point.

Figure 6 shows the hydrogen desorption curves of $LiBH_4$@NPC-4 nm. The measurements were performed using a fixed-volume Sieverts-type apparatus. We performed a series of absorption/desorption cycles at different temperatures to demonstrate that the incorporated $LiBH_4$ may be rehydrided at temperatures lower than 400 °C. All desorptions were performed at 350 °C into an initial static vacuum of 1×10^{-5} bar. Prior to each desorption, the sample was cooled to room temperature. The following sequence was performed: (1) Initial desorption at 350 °C. (2) Rehydriding at 350 °C and 60 bar H_2. (3) Second desorption at 350 °C. (4) Rehydriding at 300 °C and 60 bar H_2. (5) Third desorption at 350 °C. (6) Rehydriding at 250 °C and 60 bar H_2. (7) Fourth desorption at 350 °C. (8) Rehydriding at 350 °C and cooled to RT under 60 bar H_2. (8) Fifth desorption at 350 °C. (9) Rehydriding at 350 °C and 60 bar H_2. (10) Sixth desorption at 350 °C. As shown in Figure 6, the H_2 capacity of the sample decreased gradually with increasing cycles, and is attributed to two causes. Clearly, the lower rehydriding temperatures reduces the rate at which the sample can absorb hydrogen due to slower kinetics, and therefore the capacity fades with increasing cycling numbers. Additional capacity loss is perhaps due to sequestration of boron to the framework or simple segregation of boron. It is evident in desorption cycles 5 and 6, that upon returning to higher temperatures, the sample regains some of the capacity loss. These results indicate that the reversibility of $LiBH_4$ is kinetically inhibited at lower temperatures, and that the equilibrium hydrogen overpressure at 250 °C is still below 60 bar. Perhaps most importantly, the results demonstrate that nanoconfined $LiBH_4$ in highly ordered nanoporous carbon (NPC-4 nm) can be rehydrided at significantly improved conditions of 250 °C (below the melting point of bulk sample) and 60 bar H_2.

Finally, we address the critical issue surrounding the formation of diborane and higher borane species in the decomposition of nanoconfined $LiBH_4$. The H_2 and B_2H_6 release, per gram of infiltrated $LiBH_4$, on decomposition in different carbon templates was analyzed using a direct line-of-site residual gas analyzer mass spectrometer (RGA-MS). Figure 7 compares the B_2H_6 release and H_2 release of $LiBH_4$@CA-15 nm, $LiBH_4$@CA-9 nm and $LiBH_4$@NPC-4 nm. As indicated in the figure, more B_2H_6 is released from the decomposition of $LiBH_4$@CA-15 nm than $LiBH_4$@CA-9 nm and $LiBH_4$@NPC-4 nm. The decomposition of $LiBH_4$@NPC-4 nm shows only small release of B_2H_6. In our previous study, no measurable B_2H_6 is produced during the decomposition of $LiBH_4$@NPC-2 nm.[32]

Although the peak rate of desorption of diborane is lower than that of hydrogen, the onset of diborane and hydrogen desorption is very close. Once hydrogen desorption is well underway and the sample chemistry changes, the chemical concentrations and interactions that result in early diborane formation are evidently changed enough to reduce the amount of diborane produced. The partial pressures, per gram of infiltrated hydride, indicate the amount of diborane released during the decomposition of $LiBH_4$ decreases with decreasing pore size, and nanoconfinement can suppress or eliminate the reaction path that produces B_2H_6. These results suggest that the formation of the very stable $[B_{12}H_{12}]$-based closoborane salts, which represent thermodynamic sinks and significantly reduce the capacity and reversibility of borohydride-based materials,[9,10] can be largely mitigated through the use of nanoconfinement of the hydride. It is difficult to determine the primary cause for the change in reaction pathway, but the loss of crystallinity of the $LiBH_4$ with decreasing particle size corresponds to the changes in calorimetry and the lower temperature of decomposition onset. Without knowing the energetics of the $LiBH_4$/C interaction, we speculate this might play a role in changing the reaction pathway.

CONCLUSION

The calorimetry, H_2 release and uptake behavior, and the emission of toxic B_2H_6 have been investigated in the desorption of $LiBH_4$ confined in several pore-size carbon aerogel and highly ordered nanoporous carbon templates. In contrast to the $LiBH_4$ in carbon aerogels (CA-9 nm and CA-15 nm) $LiBH_4$ confined in the highly ordered NPC (NPC-2 nm and NPC-4 nm) did not show Bragg peaks of the crystallized $LiBH_4$, the structural or melting transition, due to the smaller pore size and subsequently induced amorphization. Nanoconfined $LiBH_4$ desorbs hydrogen

dx.doi.org/10.1021/cm103546g |*Chem. Mater.* 2011, 23, 1331–1336

at a much lower temperature with respect to bulk $LiBH_4$ and the dehydrogenation temperature decreases monotonically with the reduction of pore size. The reversibility of $LiBH_4$ was demonstrated at 60 bar H_2 and 250 °C, and may be slowly reversible under even more moderate conditions. Most importantly, mass spectroscopic analysis indicates nanoconfinement can suppress or eliminate diborane release, implying that the reaction pathway leading to higher borane species by decomposing borohydrides may be controlled. This represents a major breakthrough in the reversibility of borohydrides for hydrogen storage, as the formation of very stable closoborane species, such as $B_{12}H_{12}$ salts may be interrupted, and removed from the reaction pathway, opening the door to lightweight, reversible, boron-based hydrogen storage systems.

■ ASSOCIATED CONTENT

Supporting Information. Nitrogen sorption isotherms, X-ray diffraction patterns, FT-IR spectra, and TGA plots (PDF). This material is available free of charge via the Internet at http://pubs.acs.org.

■ AUTHOR INFORMATION

Corresponding Author
*E-mail: majzoube@umsl.edu.

■ ACKNOWLEDGMENT

This work was funded by the U.S. Department of Energy in the Hydrogen, Fuel Cells, and Infrastructure Technologies Program through the office Energy Efficiency and Renewable Energy under Contract DE-AC04-94AL85000. We are grateful to Dr. David Osborn and Dr. Dan Zhou for assistance with TEM measurement.

■ REFERENCES

(1) Schlapbach, L.; Züttel, A. *Nature* **2001**, *414*, 353.
(2) Ritter, J. A.; Ebner, A. D.; Wang, J.; Zidan, R. *Mater. Today* **2003**, *6*, 18.
(3) Mandal, T. K.; Gregory, D. H. *Annu. Rep. Prog. Chem., Chem., Sect. A* **2009**, *105*, 21.
(4) Graetz, J. *Chem. Soc. Rev.* **2009**, *38*, 73.
(5) Chen, P.; Zhu, M. *Mater. Today* **2008**, *12*, 36.
(6) Orimo, S.; Nakamori, Y.; Eliseo, J. R.; Züttel, A.; Jensen, C. M. *Chem. Rev.* **2007**, *107*, 4111.
(7) Orimo, S.; Nakamori, Y.; Kitahara, G.; Miwa, K.; Ohba, N.; Towata, S.; Züttel, A. *J. Alloys.Compd.* **2005**, *404−406*, 427.
(8) Kostka, J.; Lohstroh, W.; Fichtner, M.; Hahn, H. *J. Phys. Chem. C* **2007**, *111*, 14026.
(9) Hwang, S. J.; Bowman, R. C., Jr.; Reiter, J. W.; Rijssenbeek, J.; Soloveichik, G. L.; Zhao, J. C.; Kabbour, H.; Ahn, C. C. *J. Phys. Chem. C* **2008**, *112*, 3164.
(10) Ozolins, V.; Majzoub, E. H.; Wolverton, C. *J. Am. Chem. Soc.* **2009**, *131*, 230.
(11) Au, M.; Jurgensen, A. R.; Spencer, W. A.; Anton, D. L.; Pinkerton, F. E.; Hwang, S. J.; Kim, C.; Bowman, R. C., Jr. *J. Phys. Chem. C* **2008**, *112*, 18661.
(12) Vajo, J. J.; Skeith, S. L.; Mertens, F. *J. Phys. Chem. B* **2005**, *109*, 3719.
(13) Yang, J.; Sudik, A.; Wolverton, C. *J. Phys. Chem. C* **2007**, *111*, 19134.
(14) Au, M.; Jurgensen, A. *J. Phys. Chem. B* **2006**, *110*, 7062.
(15) Mauron, P.; Buchter, F.; Friedrichs, O.; Remhof, A.; Bielmann, M.; Zwicky, C. N.; Züttel, A. *J. Phys. Chem. B* **2008**, *112*, 906.
(16) Miwa, K.; Ohba, N.; Towata, S.; Nakamori, Y.; Orimo, S. *J. Alloys Compd.* **2005**, *404- 406*, 140.
(17) Friedrichs, O.; Remhof, A.; Hwang, S. J.; Züttel, A. *Chem. Mater.* **2010**, *22*, 3265.
(18) Zhang, S.; Gross, A. F.; Van Atta, S. L.; Lopez, M.; Liu, P.; Ahn, C. C.; Vajo, J. J.; Jensen, C. M. *Nanotechnology* **2009**, *20*, 204027.
(19) Fichtner, M. *Nanotechnology* **2009**, *20*, 204009.
(20) Adelhelm, P.; Gao, J.; Verkuijlen, M. H. W.; Rongeat, C.; Herrich, M.; van Bentum, P. J. M.; Gutfleisch, O.; Kentgens, A. P. M.; deJong, K. P.; de Jongh, P. E. *Chem. Mater.* **2010**, *22*, 2233.
(21) Nielsen, T. K.; Manickam, K.; Hirscher, M.; Besenbacher, F.; Jensen, T. R. *ACS Nano* **2009**, *3*, 3521.
(22) Gutowska, A.; Li, L.; Shin, Y.; Wang, C. M.; Li, X. S.; Linehan, G. C.; Smith, R. S.; Kay, B. D.; Schmid, B.; Shaw, W.; Gutowski, M.; Autrey, T. *Angew. Chem.* **2005**, *117*, 3644.
(23) Wagemans, R. W. P.; van Lenthe, J. H.; de Jongh, P. E.; Jos van Dillen, A.; de Jong, K. P. *J. Am. Chem. Soc.* **2005**, *127*, 16675.
(24) Paskevicius, M.; Sheppard, D. A.; Buckley, C. E. *J. Am. Chem. Soc.* **2010**, *132*, 5077.
(25) Lohstroh, W.; Roth, A.; Hahn, H.; Fichtner, M. *ChemPhysChem.* **2010**, *11*, 789.
(26) Gao, J.; Adelhelm, P.; Verkuijlen, M. H. W.; Rongeat, C.; Herrich, M.; van Bentum, P. J. M.; Gutfleisch, O.; Kentgens, A. P. M.; de Jong, K. P.; de Jongh, P. E. *J. Phys. Chem. C* **2010**, *114*, 4675.
(27) Gross, A. F.; Vajo, J. J.; Van Atta, S. L.; Olson, G. L. *J. Phys.Chem. C* **2008**, *112*, 5651.
(28) Ngene, P.; Adelhelm, P.; Beale, A. M.; de Jong, K. P.; de Jongh, P. E. *J. Phys. Chem. C* **2010**, *114*, 6163.
(29) Cahen, S.; Eymery, J. B.; Janot, R.; Tarascon, J. M. *J. Power Sources* **2009**, *189*, 902.
(30) Shane, D. T.; Corey, R. L.; McIntosh, C.; Rayhel, L. H.; Bowman, R. C., Jr.; Vajo, J. J.; Gross, A. F.; Conradi, M. S. *J. Phys. Chem. C* **2010**, *114*, 4008.
(31) Nielsen, T. K.; Bösenberg, U.; Gosalawit, R.; Dornheim, M.; Cerenius, Y.; Besenbacher, F.; Jensen, T. R. *ACS Nano* **2010**, *4*, 3903.
(32) Liu, X.; Peaslee, D.; Jost, C. Z.; Majzoub, E. H. *J. Phys. Chem. C* **2010**, *114*, 14036.
(33) Meng, Y.; Gu, D.; Zhang, F.; Shi, Y.; Cheng, L.; Feng, D.; Wu, Z.; Chen, Z.; Wan, Y.; Stein, A.; Zhao, D. *Chem. Mater.* **2006**, *18*, 4447.